Opto-Electronic
Advances

CN 51−1781/TN ISSN 2096−4579 (Print) ISSN 2097−3993 (Online)

Wearable photonic smart wristband for cardiorespiratory function assessment and biometric identification

Wenbo Li, Yukun Long, Yingyin Yan, Kun Xiao, Zhuo Wang, Di Zheng, Arnaldo Leal-Junior, Santosh Kumar, Beatriz Ortega, Carlos Marques, Xiaoli Li and Rui Min

Citation: Li WB, Long YK, Yan YY, et al. Wearable photonic smart wristband for cardiorespiratory function assessment and biometric identification. *Opto-Electron Adv* **8**, 240254(2025).

https://doi.org/10.29026/oea.2025.240254

Received: 26 October 2024; Accepted: 3 March 2025; Published online: 29 April 2025

Related articles

Opto-Electronic Advances

Article

May 2025, Vol. 8, No. 5

DOI: 10.29026/oea.2025.240254 CSTR: 32247.14.oea.2025.240254

Wearable photonic smart wristband for cardiorespiratory function assessment and biometric identification

Wenbo Li[1,2†], Yukun Long[2,3†], Yingyin Yan[4], Kun Xiao[4], Zhuo Wang[4], Di Zheng[1*], Arnaldo Leal-Junior[5,6], Santosh Kumar[7], Beatriz Ortega[8], Carlos Marques[9,10], Xiaoli Li[2,3,11] and Rui Min[2,3,11*]

Personalized health services are of paramount importance for the treatment and prevention of cardiorespiratory diseases, such as hypertension. The assessment of cardiorespiratory function and biometric identification (ID) is crucial for the effectiveness of such personalized health services. To effectively and accurately monitor pulse wave signals, thus achieving the assessment of cardiorespiratory function, a wearable photonic smart wristband based on an all-polymer sensing unit (All-PSU) is proposed. The smart wristband enables the assessment of cardiorespiratory function by continuously monitoring respiratory rate (RR), heart rate (HR), and blood pressure (BP). Furthermore, it can be utilized for biometric ID purposes. Through the analysis of pulse wave signals using power spectral density (PSD), accurate monitoring of RR and HR is achieved. Additionally, utilizing peak detection algorithms for feature extraction from pulse signals and subsequently employing a variety of machine learning methods, accurate BP monitoring and biometric ID have been realized. For biometric ID, the accuracy rate is 98.55%. Aiming to monitor RR, HR, BP, and ID, our solution demonstrates advantages in integration, functionality, and monitoring precision. These enhancements may contribute to the development of personalized health services aimed at the treatment and prevention of cardiorespiratory diseases.

Keywords: personalized health services; all-polymer sensing unit; respiratory rate; heart rate; blood pressure; biometric ID; cardiorespiratory diseases

Li WB, Long YK, Yan YY et al. Wearable photonic smart wristband for cardiorespiratory function assessment and biometric identification. *Opto-Electron Adv* **8**, 240254 (2025).

[1]Center for Information Photonics and Communications, School of Information Science and Technology, Southwest Jiaotong University, Chengdu 611756, China; [2]Department of Psychology, Faculty of Arts and Sciences, Beijing Normal University, Zhuhai 519087, China; [3]Faculty of Psychology, Beijing Normal University, Beijing 100875, China; [4]Department of Physics, Faculty of Arts and Sciences, Beijing Normal University, Zhuhai 519087, China; [5]Graduate Program in Electrical Engineering, Federal University of Espírito Santo, Fernando Ferrari Avenue, Vitoria 29075-910, Brazil; [6]Department of Cybernetics and Biomedical Engineering, VSB—Technical University of Ostrava, Ostrava, Czech Republic; [7]Centre of Excellence for Nanotechnology, Department of Electronics and Communication Engineering, Koneru Lakshmaiah Education Foundation, Vaddeswaram, Andhra Pradesh-522302, India; [8]ITEAM Research Institute, Universitat Politècnica de València, Valencia 46022, Spain; [9]CICECO-Aveiro Institute of Materials, Physics Department, University of Aveiro, Aveiro 3810-193, Portugal; [10]Department of Physics, Faculty of Electrical Engineering and Computer Science, VSB-Technical University of Ostrava, Ostrava, Czech Republic; [11]Center for Cognition and Neuroergonomics, State Key Laboratory of Cognitive Neuroscience and Learning, Beijing Normal University, Zhuhai 519087, China.

†These authors contributed equally to this work.

*Correspondence: D Zheng, E-mail: dzheng@swjtu.edu.cn; R Min, E-mail: ruimin@bnu.edu.cn

Received: 26 October 2024; Accepted: 3 March 2025; Published online: 29 April 2025

Introduction

Cardiorespiratory function assessment and biometric identification (ID) contribute to the assessment of individual respiratory and cardiac diseases to achieve personal health management[1,2]. Respiratory diseases such as different types of influenza[3], pneumonia[4], and sleep apnea syndrome[5] and cardiac diseases such as high blood pressure[6], coronary heart disease[7], and heart attack[8] also occur frequently in our lives. It is crucial to detect, diagnose, and intervene early with respiratory and cardiac disorders by monitoring cardiorespiratory function for personalized health assessment and significantly reducing the risk of mortality related to these diseases. Traditional methods of monitoring cardiorespiratory function typically require specialized and bulky types of equipment such as cardiac ultrasound machines[9], electrocardiographs[10], and CT examinations[11]. Normally, these approaches require patients to visit healthcare facilities, that cannot accurately identify personal information, and record the historical information, leading to difficulties in prompt diagnosis and accurate treatment. With the advancement of modern society and the growing need for personalized medicine, the demand for real-time, accurate, and portable smart health monitoring devices for biometric ID and cardiorespiratory function assessment is increasing significantly[12−16].

In recent years, there has been rapid development in flexible electronic devices combined with artificial intelligence (AI) for biometric ID and cardiorespiratory function assessment, to drive advances for the diagnosis and precision treatment of individual respiratory and cardiac diseases[17−20]. Xu et al. presented self-powered flexible electronic devices with 1D output for multifunctional input detection, and its functions including letter recognition, biometric ID, and digit pattern detection. This research constructed a 1D convolutional neural network with ID recognition accuracy of 96.3%[21]. Maddirala et al. reported flexible and skin-compliant capacitive pressure devices with high sensitivity, introducing air chambers into elastomeric polydimethylsiloxane (PDMS) substrate to successfully monitor cardiorespiratory function[22]. Kireev et al. proposed a wearable continuous blood pressure (BP) monitoring platform based on flexible electrical bioimpedance devices and utilized atomically thin, self-adhesive, lightweight, and unobtrusive graphene electronic tattoos as a bioelectronic interface for the human body to monitor arterial BP[23].

Although flexible electronic devices have made significant advancements in recent years, traditional flexible electrical devices often encounter difficulties when operating in specific scenarios. These devices can be susceptible to electromagnetic field interference and lack sufficient resistance to electrochemical corrosion. In contrast, optical fiber sensors have shown superior performance in such specific scenarios, owing to their immunity to electromagnetic interference and resistance to electrochemical corrosion[24,25]. Furthermore, optical fiber sensors possess several other advantages in different applications[26−28], including high sensitivity, electrical safety, flexibility, rapid response time, and biocompatibility[29]. Owing to the aforementioned advantages, optical fiber sensors are promising for applications in the monitoring of cardiorespiratory function and biometric ID[30−35]. Guo et al. developed a novel sensor featuring a multimode silica optical fiber-stretchable optical fiber-multimode silica optical fiber structure. This sensor, utilizing the Beer-Lambert Law as its sensing principle, successfully achieved precise human motion detection[36]. Li et al. developed a wearable optical fiber sensor that integrates a U-shaped micro-nano optical fiber with a flexible soft liquid sac, enabling precise monitoring of human physiological signals, including pulse signals and respiration rates[37]. Zhu et al. developed a stretchable and ultrathin optical fiber sensor, featuring wavy ultrafine optical fibers embedded within ultra-thin PDMS films, thereby enabling the creation of a flexible sensor for monitoring cardiorespiratory functions[38]. Pang et al. presented a dual-channel single-mode-multimode-single-mode (SMS) optical fiber sensor, enclosed in PDMS, which is capable of simultaneously monitoring brachial and radial arteries for the accurate prediction of BP[39]. Additionally, Li et al. designed a smartwatch integrated with an optical fiber sensor, utilizing a polyethylene (PE) tube, an air core, and two multimode silica optical fibers (MMF) to provide continuous and precise BP monitoring[40]. Wang et al. introduced an optical micro-nano fiber (MNF) sensor designed for biometric ID, which operates through the concurrent measurement of fingerprint signals. This sensor demonstrated the ability to recognize 400 sets of fingerprint data with an accuracy of 95.75%[41]. In addition to these sensors utilizing silica optical fibers, other proposals employ polymer optical fibers (POF), such as Li et al. developed stretchable optical waveguides by integrating elastomers of varying refractive indices into single fibers, enabling applications in robot finger posture and pressure sensing[42]. Wang et al., who developed a novel wearable optical microfiber intelligent sensor based on a wave-shaped polymer optical microfiber (WPOMF) for enhanced cardiorespiratory and behavioral monitoring, demonstrating high sensitivity, stability, and the potential for integration with AI technology for applications in medical rehabilitation, health monitoring, and the Internet of Things[43]. Kuang et al. developed a smart photonic wristband that incorporates POF into a sports wristband. This device achieved a pulse wave measurement error of 3.7% and successfully recognized gestures with an accuracy of 95%[44].

While these optical fiber sensors demonstrate impressive performance, there remains significant room for enhancement. The majority of contemporary optical fiber sensors are fabricated using silica optical fibers or POFs. Silica optical fiber sensors, in contrast to their POF counterparts, exhibit limitations in adaptability and biocompatibility, which consequently restrict their scope of application[45]. Furthermore, damaged silica optical fibers may pose a potential harm to human tissue[46], raising concerns about user safety, particularly during prolonged usage. Regarding POF sensors, although they possess acceptable transmission performance, their performance under strain is often suboptimal[47]. In contrast, extensible POFs demonstrate favorable strain tolerance and polymers doped with solid crystalline compounds like phosphors can open a large number of applications[48]. However, their transmission loss remains unsatisfactory[49]. Additionally, many of the existing studies lack comprehensive functionality and integration. The development of a device capable of simultaneously delivering long-term, real-time cardiorespiratory function assessment and biometric ID would significantly advance its applicability in the realm of personalized healthcare services.

Targeting all these existing problems, in this work, we propose and experimentally evaluate a wearable photonic smart wristband with the capability of cardiorespiratory function assessment and biometric ID. The core sensing unit of the smart wristband consists of POFs and a Solaris polymer optical fiber (SPOF), forming a POF-SPOF-POF (PSP) structure. The smart wristband incorporates a PSP, Dragon Skin 10 covers (DSCs), and a glycerol-filled capsule, all contributing to the all-polymer sensing unit (ALL-PSU). This all-polymer designed and integrated sensor manufacturing method merges the acceptable transmission loss of POFs with the favorable strain tolerance of extensible materials, ensuring ultrafast response and recovery times of 6 ms and 12 ms, respectively. The wristband exhibits outstanding long-term stability and durability, maintaining exceptional performance under diverse conditions, including bending, stretching, and repetitive strain over 1000 cycles, along with effective waterproofing and minimal positional drift, ensuring reproducibility regardless of the wristband's position on the wrist. Upon acquiring precise pulse wave signals, the power spectral density (PSD) analysis method is employed to estimate RR and HR with high accuracy. Distinct features of the pulse wave signals are extracted and used as inputs for machine learning models, including gated recurrent unit (GRU) neural networks and random forest (RF) algorithms, for BP estimation and biometric ID, respectively. The smart wristband demonstrated robust performance across various application scenarios, including different physical activities such as squatting, burpees, and high-knee exercises, as well as among subjects with different body mass index (BMI) profiles while offering continuous and real-time monitoring capabilities. This wearable photonic smart wristband not only allows for precise estimations of RR, HR, and BP but also demonstrates significant capability for biometric ID, highlighting its applicability in personal health services aimed at the treatment and prevention of cardiorespiratory diseases.

Methodology

Schematic of the smart wristband

The functional architecture of the smart wristband is illustrated in Fig. 1, encompassing five primary components: the sensing unit, signal acquisition, signal preprocessing, machine learning analysis, and PSD analysis. The ALL-PSU was designed to detect the vibrations induced by alteration in arterial blood flow within the radial artery, with the sensed signals transmitted to a PC. The PC was equipped with data processing algorithms, feature extraction techniques, and neural networks to enable accurate monitoring of HR, RR, BP, and ID. The monitoring results were transmitted wirelessly in real time back to the smart wristband and displayed on the screen. Additionally, the data were wirelessly sent to a customized mobile app on a cell phone, allowing for real-time and continuous monitoring in daily life. Specifically, with the objective of obtaining high-quality pulse wave signals, wavelet analysis is employed to analyze the original signals during the signal acquisition phase.

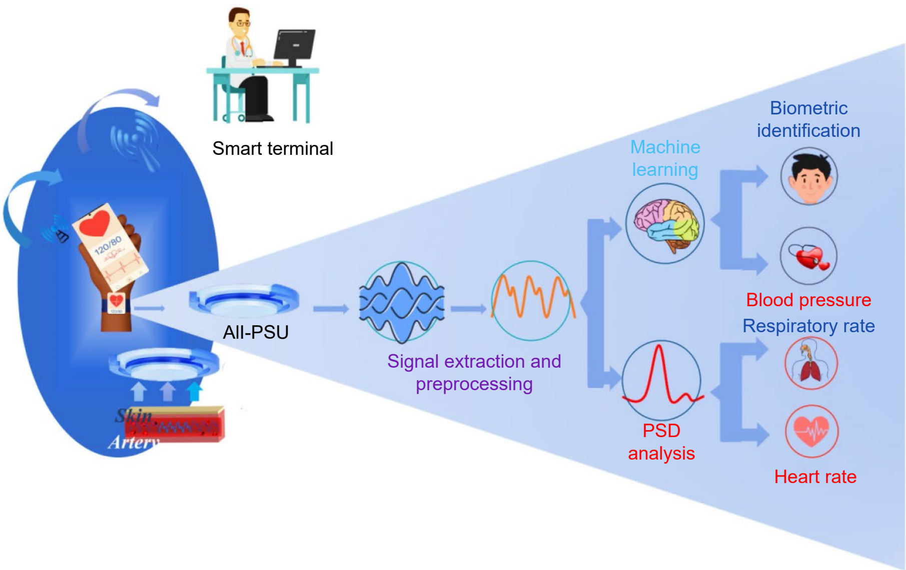

Fig. 1 | Functional architecture of the proposed wristband, including mainly five primary components: the ALL-PSU sensing unit, signal extraction and preprocessing, machine learning models, and PSD analysis.

Following the initial signal acquisition, the signals undergo preprocessing, involving the application of a band-pass filtering algorithm to purify the acquired signals, resulting in the extraction of clean pulse wave signals. Additionally, a peak-seeking algorithm is applied to extract the RR and HR signals from the pulse wave signals. The machine learning analysis component is focused on biometric ID and BP estimation. Utilizing features extracted from the pulse wave signals, the RF and GRU neural network models are employed to achieve precise biometric ID and BP estimation, respectively. The effectiveness of the machine learning analysis component has been demonstrated through its accurate ID of subjects across different BMI categories and precise monitoring of BP after various activities, including relaxation, squatting, and burpee jumping. Through the utilization of fast fourier transform (FFT) techniques to extract the frequencies of RR and HR from the signals and enable precise calculation of RR and HR parameters, PSD analysis facilitates continuous surveillance of cardiorespiratory function. This method demonstrates robust performance across a spectrum of physical activities, including squats, burpee jumps, and high knees. The smart wristband is equipped with a display interface for real-time presentation of ID, BP, RR, and HR information. Additionally, it is capable of transmitting data to a computing platform, allowing healthcare professionals to analyze the collected physiological information and provide personalized health services to the users.

Design and fabrication of the All-PSU

To monitor pulse wave signals, a PSP fiber adapter utilizing a polyurethane elastomer known as Solaris, notable for its high refraction (refer to Table S1), has been developed. This elastomer is injected into a silicone tube (inner diameter 300 μm) of specific dimensions to create a sensing zone characterized by high elasticity and chemical stability. Following this, the Solaris-filled silicone tube is integrated with two POFs which with an inner diameter of 250 μm, as the PSP fiber adapter. This designation enhances optical coupling and enables the PSP fiber adapter's integration into wearable devices. The PSP fiber adapter is depicted in Fig. 2(a), where the light transmission process is also depicted through the POF, passes through the Solaris-filled silicone tube, and finally emerges from the opposite end. Leveraging the principles of the Beer-Lambert law[50], the PSP fiber adapter is engineered to identify variations in strain through the modulation of light intensity loss. When the light transmits through the Solaris-filled silicone tube, the reduction in light intensity can be calculated by:

$$A = \log_{10}\left(\frac{I_0}{I}\right) = \varepsilon lc\ , \tag{1}$$

where A is the absorbance, I_0 is the initial intensity, I is the transmitted intensity, ε is the molar absorptivity, l is the length of the light path and c is the concentration of the solution of the Solaris. Since the parameters ε and c remain constant, A and is directly proportional to l.

The shape of the silicone tube will change due to pres-

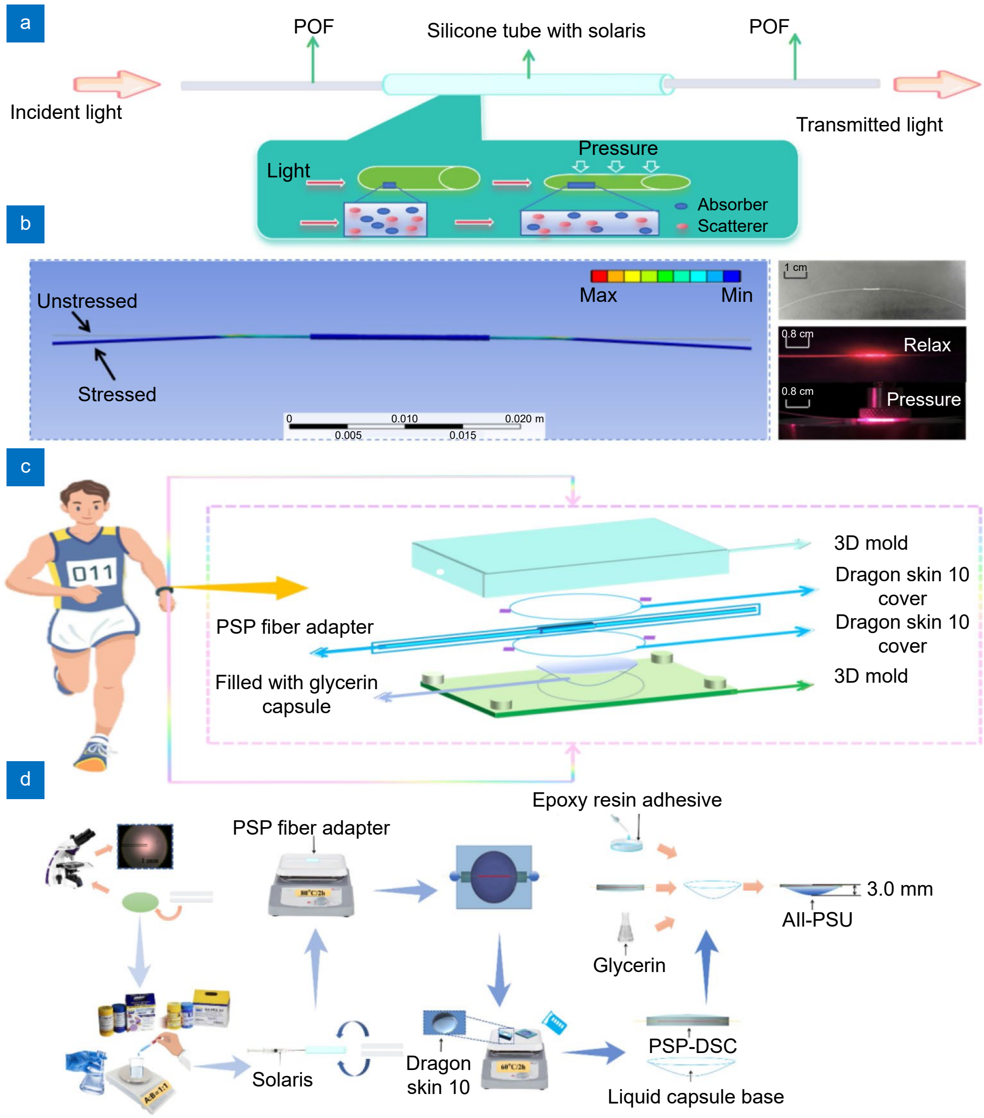

Fig. 2 | (**a**) The conceptual figure of the PSP fiber adapter. (**b**) Pressure simulation (left) alongside the actual configuration of the PSP fiber adapter (right), demonstrating the adapter's response to pressure. (**c**) Exploded schematic of the practical All-PSU, including 3D molds, DSCs, PSP fiber adapter, and a glycerol-filled capsule. (**d**) Structural diagram of the All-PSU, the entire process of All-PSU is divided into three parts: the PSP fiber adapter fabrication, the PSP-DSC and liquid capsule base fabrication, and the All-PSU construction and coating.

sure, bending and strain. Consequently, the length of light path will also be affected. Assume Δl represents the variation in the length of the light path, the corresponding change in absorbance can be calculated using the following equation:

$$\Delta A = \log_{10}\left(\frac{I}{I-\Delta I}\right) = \varepsilon \Delta l c \ , \tag{2}$$

where ΔA is the variation of the absorbance and ΔI is the variation of the intensity. To facilitate the measurement of light intensity, a light power meter is utilized in the experiments. Since the power of light can be calculated by: $P = IS$ (Where P (mW) is the light power, S is the area), the power level (decibel relative to one milliwatt) can be calculated by

$$x = 10 \cdot \log_{10}\left(\frac{P}{1\ \mathrm{mW}}\right) \ , \tag{3}$$

where x (dBm) is power level. $P \propto I$, $\log_{10} I$ has linear relationship with l (according to Eq. (1)), therefore x has linear relationship with l, as illustrated by the following equations

$$-\frac{1}{10}x + \log_{10}\left(\frac{I_0 S}{1\ \mathrm{mw}}\right) = \varepsilon l c \ , \tag{4}$$

$$x = -10\left(\varepsilon l c - \log_{10}\frac{P_0}{1\ \mathrm{mw}}\right) \ , \tag{5}$$

$$x = -10\varepsilon lc + x_0 \,, \tag{6}$$

where P_0 (mw) represents the initial light power, x_0 (dBm) represents the initial power level. Consequently, when a variation occurs in the length of the light path, the variation in x is directly proportional to the variation in the length of light path, which can be illustrated as: $\Delta x = -10\varepsilon \Delta lc$.

This conclusion represents the sensing principle of the PSP fiber adapter, enabling it to detect vibrations caused by the human wrist pulse. However, considering real-world sensing scenarios, external forces can also deform the geometry of connection joints of POF and stretchable optical fiber, as shown in Fig. 2(b), causing light coupling loss at these points. This phenomenon affects the linear relationship between changes in the light path length and the resulting light power loss, which can be illustrated as: $\Delta x = -10\varepsilon \Delta lc + \alpha(\Delta l)$, where $\alpha(\Delta l)$ represents the light power loss at the connection parts. Guo et al. employed the dual-wavelength difference method to mitigate the effect of light coupling loss[36]. In our work, to address the same issue, a different approach is employed, which an "ear-type" structure was designed to enhance the durability of the connection joints, thereby significantly reducing light coupling loss at these joints. This design can effectively eliminate the light coupling loss and has been proved by the experimentation, which will be detailed in the characterization testing section.

The PSP structure, which features an all-polymer structure with high integration and inspired by several representative existing works in this area[36,40]. Inspired by the work of Guo et al., our sensor choosing the Beer-Lambert Law as our sensing principle due to its highly linear relationship between external forces causing changes in the length of the light path and the resulting light power loss. To achieve this, the Solaris was employed as the macroscopically homogeneous medium to absorb light. As demonstrated in Table S1, Solaris was selected for its superior stretchability compared to other materials. Inspired by the work of Li et al., we utilized a silicone tube as the encapsulation structure of the Solaris materials. As shown in Table S2, silicone was selected for its superior stretchability compared to tubes made from other materials. Consequently, the SPOF in our sensor comprises a silicone tube filled with Solaris material, with POFs employed to transmit the input and output beams. As aforementioned, an "ear-type" structure was designed to enhance the durability of the connection joints of this SPOF and the POFs, thereby significantly reducing light coupling loss at these joints. Liquid capsule bases are widely used in both electronic and optical sensors due to their ability to expand the sensing zone based on Pascal's Principle[51]. Consequently, our sensor incorporates a glycerol-filled capsule base to leverage this advantage. The actual configuration of the PSP fiber adapter is also depicted in Fig. 2(b), illustrating its response to pressure, including the resulting strain and relaxation. The exploded schematic of the All-PSU is visually detailed in Fig. 2(c). This unit is designed using two 3D-printed molds, dual DSCs, a precision-engineered PSP fiber adapter, and a glycerol-filled capsule. The combination of these components enables the precise detection of subtle skin surface strain, with the PSP fiber adapter playing a pivotal role in this function. Aside from the PSP fiber adapter, the other components also play significant roles in the All-PSU. The meticulously designed 3D-printed molds serve a dual purpose: they not only provide structural integrity but also protect the All-PSU from any mechanical disturbance caused by wrist movements, ensuring the sensitivity of All-PSU and the accuracy of extracting pulse wave signals. The DSCs were designed using Dragon Skin 10 for its Young's modulus, which closely resembles that of human tissue, ensuring excellent biocompatibility. As for the glycerol-filled capsule, it is strategically positioned to extend through a central aperture in the 3D mold, making direct contact with the skin. This design allows a single liquid capsule to span 2–3 adjacent tendons, enlarging the effective sensing area and minimizing crosstalk, which results in high-fidelity acquisition of pulse wave signals.

The fabrication of the All-PSU, as depicted in Fig. 2(d), involves a series of precise steps. Initially, an integrated preparation process was employed to fabricate the PSP structure, ensuring the consistent performance of our sensors. Two POFs are meticulously polished using grinding sandpaper to attain flat end faces, after which components Solaris A and B are blended, followed by a 15 minute degassing process, and the degassed precursor solution is then injected into a siliconetube. The POFs are then inserted into the tube containing the precursor solution to assemble the PSP fiber adapter. Following the assembly procedure outlined above, the PSP fiber adapter undergoes a 2 hour curing process within a temperature-regulated heating platform maintained at 80 °C, thereby finalizing its fabrication. To enhance the stability of the PSP fiber adapter, ultraviolet glue is applied to seal the connection between the POFs and the tube. Subsequent to this, the PSP fiber adapter is encased with DSC, each 500 μm thick, to form the PSP-DSC. For the glycerol-filled capsule, equal parts of Dragon Skin 10 A and B are mixed, degassed for 15 minutes, and then poured into a custom mold. After curing at 60 °C for 2 hours, the base is demolding and filled with glycerol, a chemically stable and non-toxic material. Finally, the glycerol-filled capsule and the PSP-DSC are meticulously sealed together using a high-strength epoxy adhesive, culminating in the formation of the All-PSU. This sealing technique not only ensures a robust and waterproof bond but also preserves the integral sensitivity of the All-PSU.

Signals extraction and processing

During a ventricular beat, the heart undergoes constant contraction and relaxation, which causes the walls of the aortic vessels to dilate and contract. This periodic increase and decrease in blood volume creates waves of pressure changes that are transmitted as pulse wave signals[52,53]. The characteristics of pulse wave signals such as shape, period, peak, and waveform are closely related to the level of cardiorespiratory fitness[54]. When pathological changes occur, the shape of the pulse wave signals changes, which means the features embedded within these signals contain a wealth of physiological and pathological information. Obtaining clean and accurate pulse wave signals is therefore a critical prerequisite for effectively extracting these informative features. Moreover, acquiring clean and accurate signals is critical for successful cardiorespiratory function assessment, including the monitoring of RR and HR. Given the importance of these clean and accurate signals, signals preprocessing represents a crucial first step in the overall process of signals extraction and processing. The methods illustrated in Fig. 3(a) were utilized to extract clean and accurate pulse wave signals, as well as respiratory signals. To mitigate the high-frequency noise and baseline drift inherent in the raw signals, multi-scale wavelet decomposition was employed. Following this noise reduction step, the raw signals undergo further refinement through the application of bandpass filters. These filters are aimed at separating the respiratory, spanning 0.15–0.6 Hz, and pulse wave signals, spanning 0.6–3.0 Hz. Such signal preprocessing lays a solid foundation for enhancing the precision and reliability of estimations for RR, HR, BP, and biometric ID. The PSD analysis method, which plays a pivotal role in signal processing, particularly within the field of physiological information analysis, has been utilized in our study to facilitate the accurate monitoring of RR and HR. The fast fourier transform (FFT) is employed as the fundamental method underlying the PSD analysis to accurately determine the frequency components present in the preprocessed RR and HR signals, respectively. Based on the dominant frequency components identified through the FFT algorithm, the underlying physiological frequencies of the RR and HR can be determined from the largest frequency peaks present in the respective signals. Based on these frequencies, the respective RR (breaths per minute, breaths/min) and HR (beats per minute, bpm) values can be calculated as follows:

$$HR = \frac{60}{1/f_{\mathrm{HR}}} , \tag{7}$$

$$RR = \frac{60}{1/f_{\mathrm{RR}}} , \tag{8}$$

where f_{HR} (Hz) is the frequency of HR and f_{RR} (Hz) is the frequency of RR.

The PSD analysis method described above is illustrated in Fig. 3(b). As explained above, the pulse wave signals contain a wealth of physiological and pathological information embedded within their features. More concretely, as illustrated in Fig. 3(c), seven distinct features have been successfully identified and extracted from pulse wave signals, with the aim of estimating BP and biometric ID. For a comprehensive understanding of these features, including their definitions and interrelations, please refer to Table S3.

Focusing on the BP estimation, the pulse wave signals constitute a one-dimensional time series with inherent backward and forward temporal correlations. To adeptly navigate this complexity, a GRU network is introduced, which is renowned for its efficacy in the regression prediction of ordered long sequences. The GRU network has the capability to address long-standing issues and enhance global memory control through its gating structure updating mechanism[55]. As illustrated in Fig. 3(d), the GRU model architecture comprises several GRU memory blocks that share parameters, as well as fully connected layers which provide the BP output values. Thus, seven distinct features extracted from the pulse wave signals, as described previously, serve as the inputs to the model, while the outputs correspond to the predicted SBP and DBP. During the training phase, the

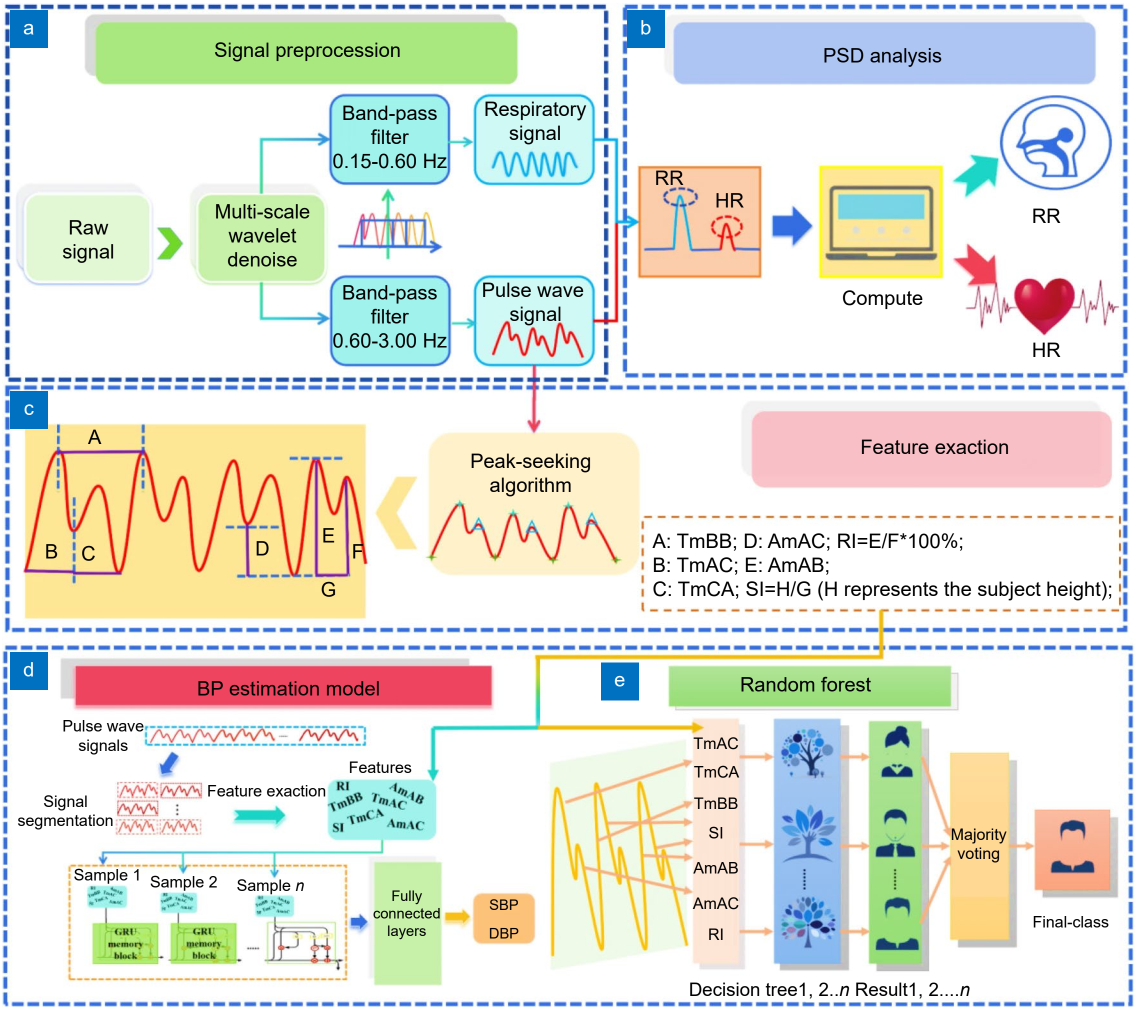

Fig. 3 | (**a**) Method to extract clean and accurate pulse wave signals as well as respiratory signals. (**b**) PSD analysis method utilized to monitor RR and HR. (**c**) Feature extraction process and the seven distinct features extracted from the pulse wave signals, which are utilized for both BP estimation and biometric ID (H represents the subject height). (**d**) Architecture of the GRU model developed for BP estimation. (**e**) Structure of the RF classifier implemented for biometric ID.

predicted SBP and DBP values are compared against the actual ground truth measurements by calculating a loss function, which is then backpropagated through the network to optimize the model parameters. The performance of the trained GRU model is subsequently evaluated in the testing phase by comparing the predicted SBP and DBP to the measured values.

With regard to finding the biometric ID, the selected RF algorithm is based on multiple decision trees that operate independently, a characteristic that significantly reduces the risk of model overfitting. This attribute makes RF particularly effective for classification-based predictive tasks. A notable advantage of employing the RF approach is its ability to handle a multitude of input features within the data without necessitating manual feature selection[56]. In our study, the input features provided to the RF model are the same seven distinct features extracted from the pulse wave signals, analogous to the inputs of the GRU model described previously. The RF model itself consists of 500 decision trees specifically designed for biometric ID. The final prediction results are aggregated from the outcomes of each individual tree, ensuring a robust and reliable biometric ID process, as illustrated in Fig. 3(e). However, the details of the experimental procedures and the RR, HR, BP and biometric ID results will be presented in the next sections.

Results and discussion

Characterization testing

To assess the performance of both the PSP-DSC and All-PSU, a series of experiments were conducted as depicted in Fig. 4(a), utilizing a Super-Luminescent Diode (PERLUM, SLD-Mcs-371-HP2-SM) as the light source and either an optical power meter (Thorlabs PM100D) or a spectrometer (THORLABS' CCS175) for signal reception. PSP-DSC was systematically positioned on a pressure platform (HPA, NK-500), and pressure increments of 10 N within the range of 0–100 N were applied using a gauge-controlled probe (Edingburgh HP-500), enabling the observation of a correlation between light loss and pressure escalation. This experiment was conducted three times, and the results are presented in Fig. 4(b). Both the pressure levels and the corresponding transmitted light power intensities were meticulously recorded. The line plot illustrates the mean value of the transmitted light power derived from the three repeated experiments, while the gray area surrounding the line plot represents the data distribution across these trials (This applies similarly to Fig. 4(d) and 4(f), which illustrated bending and stretching experiments respectively). As depicted in Fig. 4(b), a linear relationship between force and transmitted light power is observed. This finding is consistency to the afore mentioned sensing principle of the PSP adapter (refer to Eq. (7) in the Design and Fabrication of the All-PSU section of this article), exhibiting

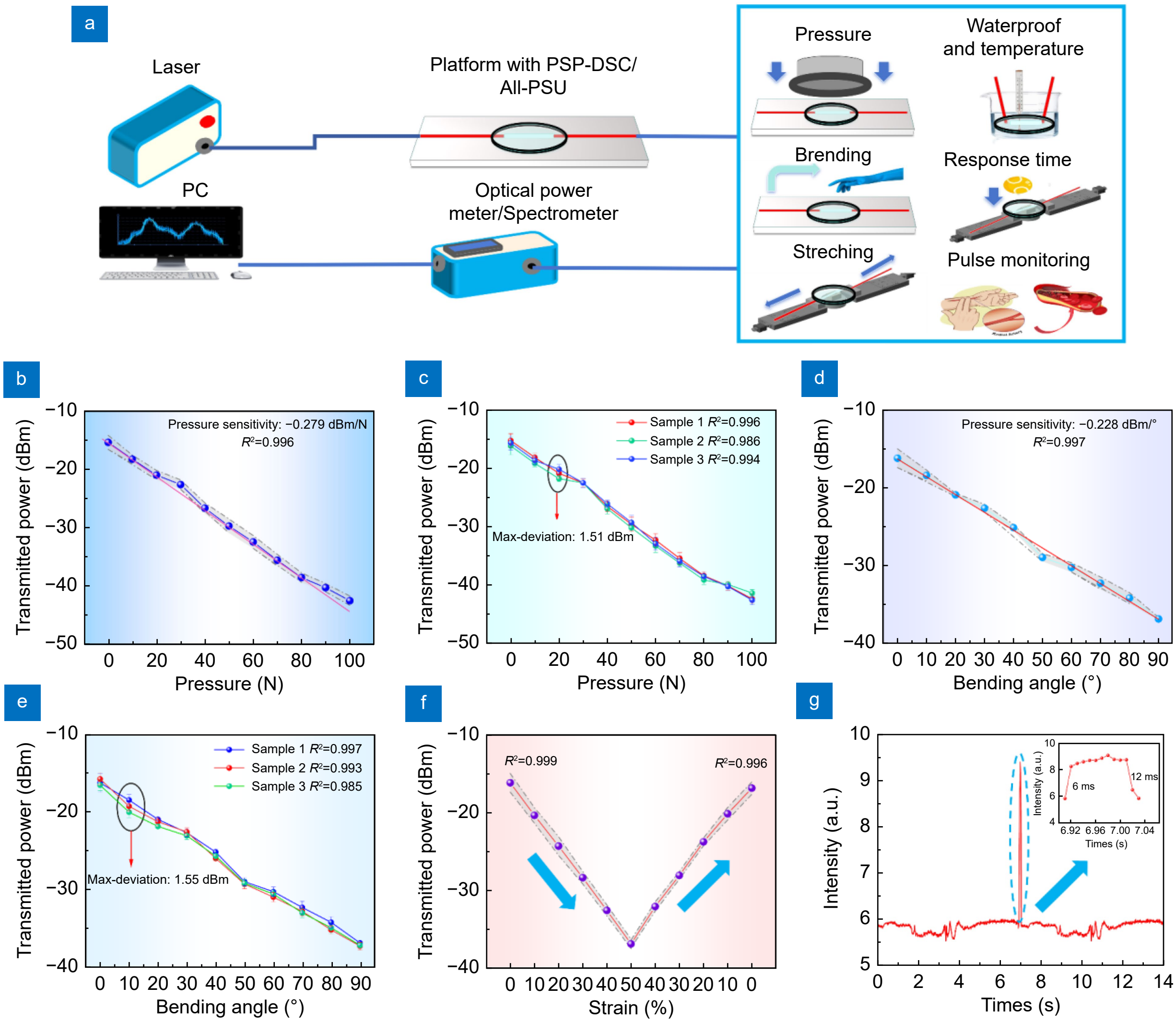

Fig. 4 | (**a**) Schematic diagram of the PSP-DSC and All-PSU performance test experiments. (**b**) Transmitted power of PSP-DSC under varying pressures, with pressure increased by 10 N each time. The line plot illustrates the mean value of the transmitted light power derived from the three repeated experiments. The gray area surrounding the line plot represents the data distribution across these trials. (This applies similarly to subfigure (d) and (f)). (**c**) Transmitted power of three PSP-DSC samples under varying pressures, with pressure increased by 10 N each time. (**d**) Transmitted power of PSP-DSC under different bending angles, with angles increased by 10° each time. (**e**) Transmitted power of three PSP-DSC samples under different bending angles, with angles increased by 10° each time. (**f**) Transmitted light power of PSP-DSC under tensile strains, with deformation increased by 10% every 30 seconds. (**g**) Transient pulse response time results (response time: 6 ms, recovery time: 12 ms).

an R^2 of 0.996 within the range of 0–100 N. The pressure sensitivity within this interval is calculated to be −0.279 dBm/N. Additionally, three PSP-DSCs were fabricated using the same methodology and subjected to identical pressure conditions. The results, depicted in Fig. 4(c), demonstrated consistent pressure performance, with a maximum deviation of 1.51 dBm in transmitted light power and closely matching R^2 under similar conditions.

In our continued exploration, further experiments focusing on the bending sensitivities of the PSP-DSC were conducted. Initially, we manually bent the PSP-DSC on a platform, starting at a 0–90 degree angle and then incrementally increasing the angle by 10 degrees process, utilizing a protractor for accurate angle measurements. This experiment was also conducted three times. These experimental results, as depicted in Fig. 4(d), reveal a decrease in the transmitted light power of the PSP-DSC with increasing bending angles. Within the bending range of 0–90 degrees, the R^2 was observed to be 0.997, indicating a distinct bending sensitivity of −0.228 dBm/°. A linear relationship between pressure and transmitted light power is observed. This finding is also consistency to the aforementioned sensing principle of the PSP adapter. Similar to the pressure condition experiment, the three aforementioned PSP-DSC samples were bent within the same range of 0–90 degrees. Figure 4(e) shows the results, indicating consistent performance with a maximum deviation of 1.55 dBm and closely matching R^2. Subsequently, the PSP-DSC's response in stretching was examined. For the three repeated trials in this test, the PSP-DSC was positioned on stepper motors (LPTA01200B LAIPER), which systematically stretched it to 50% strain, increasing the strain by 10% every 30 seconds until the recovery phase began. The stretching test results illustrated in Fig. 4(f) showed an R^2 of 0.999 and a stretching sensitivity of −0.411 dBm/% within the 0–50% strain range. During the recovery phase, the results demonstrated an R^2 of 0.996 and a stretching sensitivity of 0.400 dBm/% within the 50%–0% strain range. The linear relationship of strains and the transmitted power level also remain consistency to the sensing principle. The experiments examining the PSP-DSC's response to pressure, bending, and stretching not only demonstrated the sensitivity of the PSP-DSC but also confirmed the sensing principle in practice. Furthermore, the response and recovery time of the All-PSU were assessed through a meticulously conducted experiment involving the use of a ping-pong ball dropped from a height of 50 mm, thereby creating a transient pulse signal upon impact with the All-PSU. As illustrated in Fig. 4(g) the All-PSU exhibits a response time of 6 ms and a recovery time of 12 ms, highlighting the All-PSU's exceptional rapidity in both responding and recovering, which is crucial for real-time vital signs monitoring.

The PSP-DSC and the glycerol-filled capsule have been sealed together, resulting in the formation of the All-PSU, as described above. The functionality and durability of the All-PSU are evaluated in our experiment. The extensive applicability of the All-PSU for monitoring pulse wave signals across subjects with varying BMI categories (thin, well-balanced, and fat) and during a variety of activities (e.g., rest, squat, burpees, and high knee) has been confirmed by the experiments, as depicted in Fig. S1–S2, respectively. Figure S3 displays the radial artery pulse wave signals collected by the All-PSU before and after 30 days, showcasing its consistent performance over an extended duration. Additionally, the dynamic response of the All-PSU was evaluated across a range of tensile velocities on stepper motors, from 40% (0.783 mm/s) to 140% (2.693 mm/s), as illustrated in Fig. 5(a). To assess its operational stability and reliability over time, the All-PSU underwent cyclic tensile strain testing on the stepper motors. The results, presented in Fig. 5(b), demonstrate a slight performance degradation after 1000 cycles under a tensile strain of 50%. This finding underscores the exceptional robustness and durability of the All-PSU. As shown in Fig. 5(c), the All-PSU was immersed in water at room temperature (23 °C) for 24 hours, with its response intensity recorded every 2 hours to verify its waterproofing. The results indicate a maximum difference in response intensity change within 24 hours of 8%. Furthermore, Fig. 5(d) demonstrates the All-PSU's placement in water at various temperatures to assess temperature sensitivity. The All-PSU exhibited superior response intensity at 36.2 °C to 38.8 °C, compared to the other two temperature ranges of 14.9 °C to 21.5 °C and 54.7 °C to 60.1 °C, with maximum differences of 23.1% and 16.6%, respectively. This comprehensive analysis does not only highlight the capabilities of the PSP-DSC and All-PSU under various conditions but also underscores their potential applications in physiological information monitoring. The All-PSU's capability to monitor pulse wave signals at different locations on the wrist has been confirmed by an experiment illustrated in Fig. 5(e). On the left side of Fig. 5(e), a grid marks the wrist region, with a black rectangle representing the wrist area

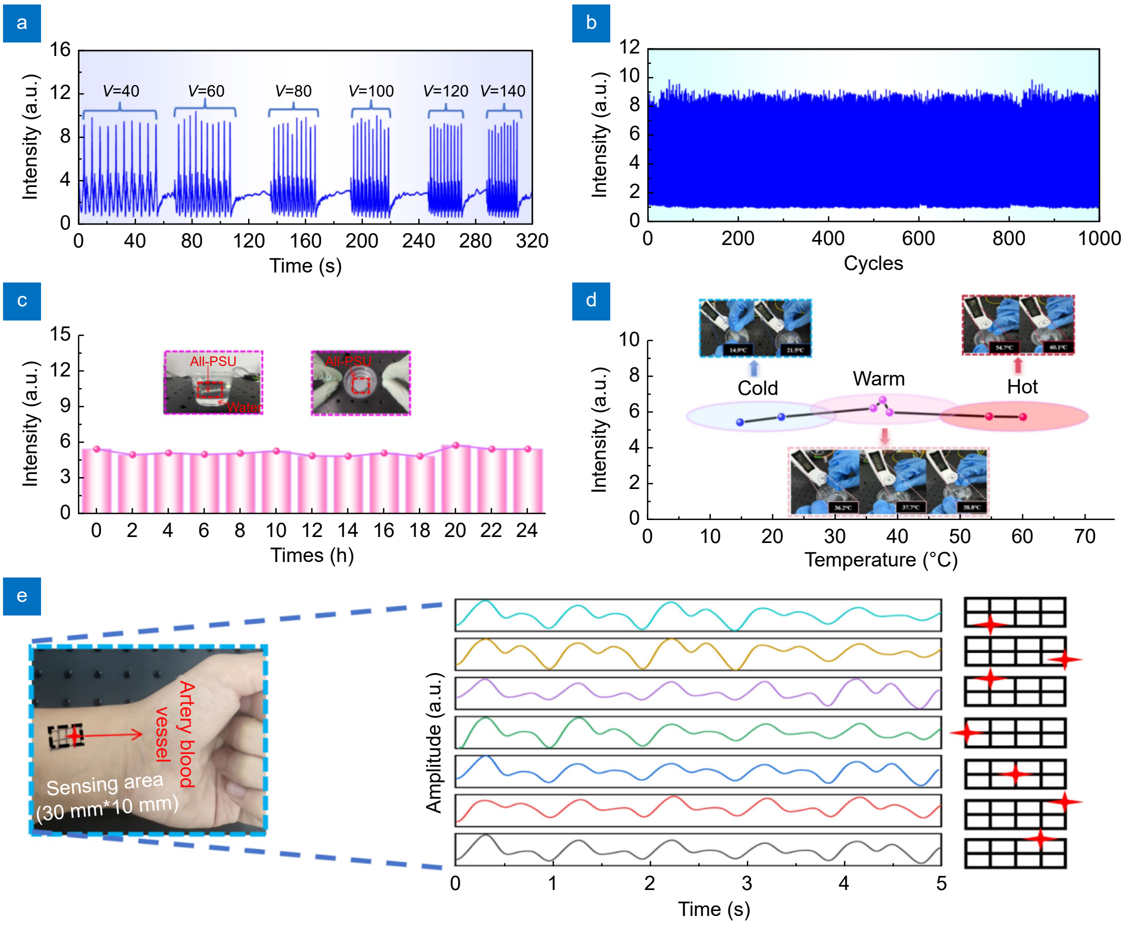

Fig. 5 | (**a**) The dynamic response of the All-PSU. Evaluated across a range of tensile velocities on stepper motors. (**b**) Performance assessment of the All-PSU through cyclic tensile strain testing, subjected to a tensile strain of 50% over 1,000 cycles. (**c**) Waterproofing of the All-PSU confirmed by immersion in water at room temperature (23 °C) for 24 hours, with response intensity recorded every 2 hours. (**d**) Response intensity of the All-PSU placed in water at various temperature. (**e**) Pulse wave signal monitoring at different wrist locations, with the star shape indicating the position of the All-PSU.

and a red pentagram indicating the All-PSU's placement. The right side of the figure confirms the successful detection of pulse wave signals at different locations without distortion due to positional drift.

The characterization tests have demonstrated that the All-PSU exhibits several notable advantages that underscore its suitability for precise physiological monitoring applications. These advantages include high sensitivity and accuracy, ultra-fast response and recovery times, remarkable long-term stability and durability, effective waterproofing, and minimal positional drift. Specifically, due to the optical sensing principle and the unique all-polymer sensor design, the All-PSU demonstrates significantly faster response and recovery times compared to traditional electrically-based pressure sensors[57,58], thereby ensuring reliable real-time pulse monitoring. Furthermore, the strong linear relationship between light power loss and varying pressures, bending angles, and tensile strains confirms the effectiveness of the "ear-type" structure design in addressing the issue of light coupling loss at the connection joints, without relying on the dual-wavelength difference method[36].

RR and HR estimation

To evaluate the smart wristband's capability to monitor RR and HR under various physiological conditions, three distinct experiments were designed, as outlined in Fig. 6(a). These experimental procedures involved four subjects exhibiting different BMI values (detailed subject information provided in Table S4), wherein their resting state RR and HR were monitored. Since pulse signals are weak, it is crucial to ensure the standardization and consistency of the measurement process. Therefore, throughout the entire experiment, each subject wore the

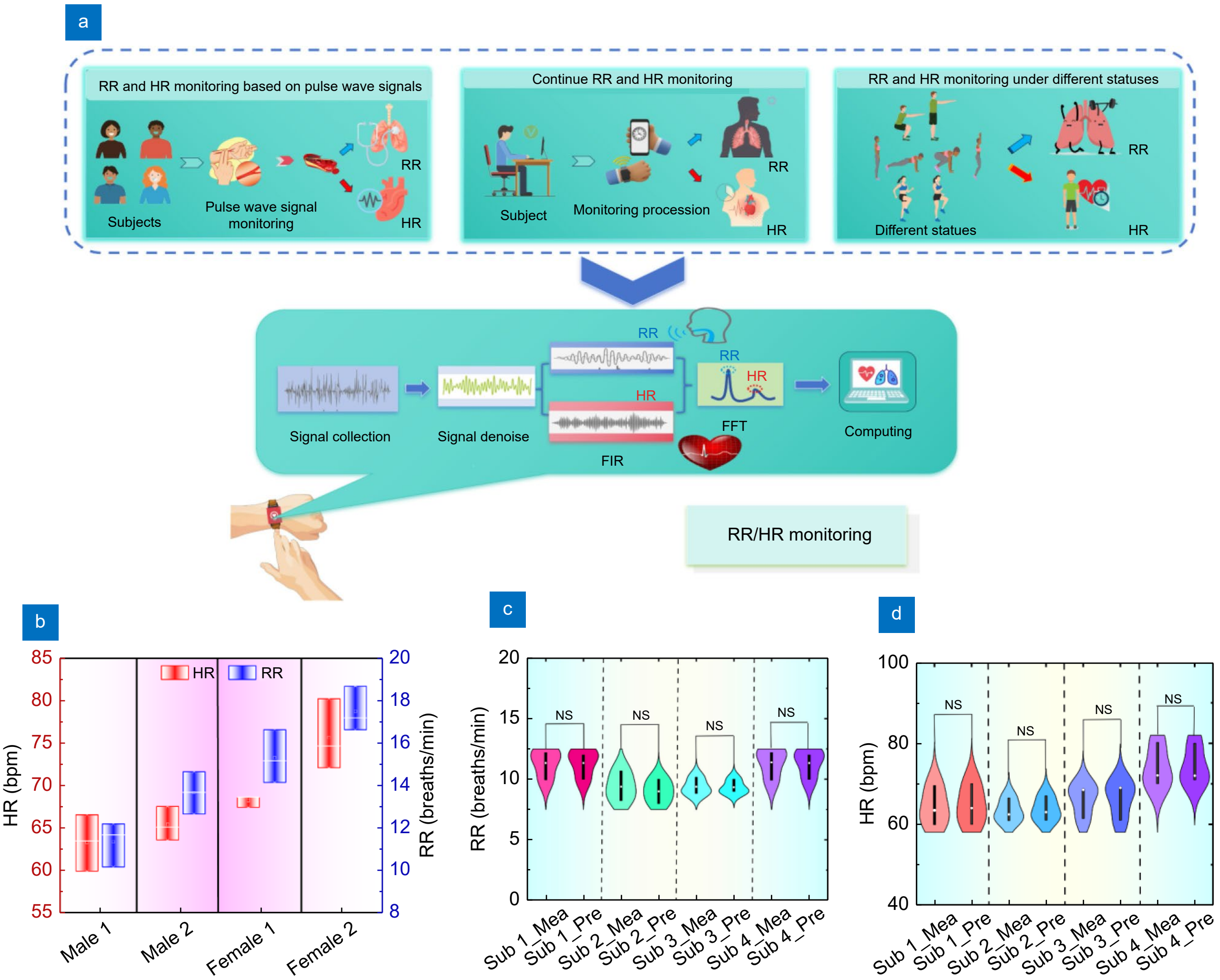

Fig. 6 | (**a**) Diagram and processing schematic of RR and HR monitoring system based on PSD analysis. The experiment was mainly divided into three stages: four subjects monitored their RR and HR under relaxed conditions, another continuously monitored his RR and HR from 14:00–18:00, and four subjects monitored their RR and HR under different states (squat. burpee and high knee). Signal processing is mainly divided into signal acquisition, signal noise reduction, signal extraction, frequency domain conversion, and RR and HR calculation. (**b**) Line box plot of the four subject's results of RR and HR for four subjects. (**c**) Violin plot of the four subjects measured and predicted RR results, and (**d**) Violin plot of the four subjects measured and predicted HR results. NS: indicates that there is no significant difference between the results of measured and predicted, indicating that the results of predicted HR, according to the proposed system, are accurate for different subjects.

proposed wristband on their wrist, and the ALL-PSU was securely fixed over the radial artery using a specially designed 3D-printed mold to capture pulse wave signals precisely. Additionally, the RR and HR of one subject were continuously tracked during unrestricted daily activities performed from 14:00 to 18:00 hours. Finally, the RR and HR of these four subjects were monitored while they engaged in different physical activities (squats, burpees, and high-knee).

In the initial experimental phase, four subjects were instructed to rest for two minutes prior to commencing the data collection. Once the subjects had attained a state of calm, their RR and HR were measured in succession, and this process was repeated three times to confirm the accuracy of the measurements. Manual counting was utilized as the reference method for RR assessment, while a heart rate monitoring belt (POLAR H10) was employed for HR measurement. Since the ECG signal is related to the pulse wave signal in terms of temporal association and physiological reflections[59–61], the ECG signal collected by POLAR H10 was employed as a reference standard to calibrate the pulse signal. Figure 6(b) illustrates the predicted RR and HR values for the participants. The mean predicted RR and HR were 11 breaths/min and 63 bpm for individuals in a lean condition, 13 breaths/min and 65 bpm for those in a proportionate condition, 15 breaths/min and 68 bpm for those in an overweight condition, and 17 breaths/min and 75 bpm for those in an obese condition, respectively. These findings corroborate previous studies suggesting a positive correlation between increased BMI and elevated RR and HR[62,63]. The Root Mean Squared Error (RMSE) and Mean Absolute Error (MAE) were calculated using Eq. (S1, S2), with the results presented in Table S5. The maximum and average RMSE for RR monitoring were 0.655 breaths/min and 0.423 breaths/min, respectively, while the corresponding MAE were 0.654 breaths/min and 0.391 breaths/min. For HR monitoring, the maximum and average RMSE were 0.571 bpm and 0.476 bpm. with MAE of 0.462 bpm and 0.411 bpm. A paired *t*-test was then conducted on these data sets[64]. As illustrated in Fig. 6(c) and 6(d), the violin plots for RR and revealed no statistically significant difference between the measured and predicted results.

After the initial experiments, the study conducted continuous RR and HR monitoring on a male participant (height: 178 cm, weight: 70 kg) over a 4 hour period (14:00–18:00) without restricting his activities. Measurements were taken 8 times per hour. Manual counting and the POLAR H10 device served as reference standards for RR and HR, respectively. Figure 7(a) displays the subject's RR and HR stability throughout the test, with average values of 14 breaths/min and 88 bpm, all within the normal range (RR: 12–20 breaths/min, HR: 60–100 bpm). The MAPE for RR and HR measurements was calculated using Eq. (S3), with the results shown in Table S6. The maximum and average MAPE for RR were 0.742% and 0.694%, and for HR were 0.712% and 0.406%. Violin plots in Fig. 7(b) and 7(c) for measured and predicted results each hour, after analysis with paired *t*-tests, demonstrated no significant difference, confirming that the predicted results matched the POLAR H10 measurements. In the third set of experiments, the RR and HR of four subjects performing three different physical activities: squats, burpees, and high knees, were monitored. Each subject began with ten squats, rested for five minutes, then performed ten burpees, rested again for five minutes, and concluded with 60 seconds of high knee.

Each activity was timed for one minute and repeated three times. The scatter and line box plots of the measured RR and HR are shown in Fig. 7(d) and 7(e). Figure 7(d) indicated an increase in RR and HR with the intensity of exercise, which is consistent with previous research[65,66]. The highest RR and HR were observed during the high knee exercise, demonstrating the wristband's ability to detect fluctuations in RR and HR across different physical states. Correlation analysis presented in Fig. 7(f) and 7(g) showed correlation coefficients of 0.95 and 0.91 for RR and HR, respectively. The MAPE was calculated using Eq. (S3) for the different activities, as illustrated in Fig. 7(h) and 7(i). The average RR, HR, and MAPE across various physical activities are illustrated as follows:

- **Squatting:** 15 breaths/min and 92 bpm, max MAPE of 6.822% and average MAPE of 5.401% for RR; max MAPE of 4.112% and average MAPE of 3.545% for HR.
- **Burpee:** 20 breaths/min and 108 bpm, max MAPE of 7.838% and average MAPE of 7.415% for RR; max MAPE of 4.307% and average MAPE of 4.032% for HR.
- **High knee:** 27 breaths/min and 123 bpm, max MAPE of 8.778% and average MAPE of 8.364% for RR; max MAPE of 4.725% and average MAPE of 4.181% for HR.

These results demonstrate that the smart wristband can effectively monitor RR and HR fluctuations during various physical activities and across subjects with different BMI values. The device's ability to consistently capture accurate physiological data in both resting and dynamic states facilitates comprehensive health monitoring during exercise. This capability not only supports fitness tracking but also provides valuable data for the development of personalized health plans. The wristband's high accuracy, demonstrated in comparison with established measurement methods such as the POLAR H10 monitor, further underscores its reliability and potential as an essential tool for continuous health assessment and early detection of health anomalies.

BP estimation

To confirm the capability of the smart wristband to monitor BP, as illustrated in Fig. 8(a), the validation process of three pivotal phases was structured, including BP monitoring modeling continuous BP monitoring, and BP monitoring under varied conditions. In the first phase, BP monitoring modeling, six subjects with diverse BMI levels were engaged to participate in the experiment (refer to Table S7). This diversity in subjects' BMI was chosen to enhance the model's generalizability. The data collection for this phase spanned one week, ensuring a comprehensive dataset was available for model training and validation. In the second phase, which consists of continuous BP monitoring, a single subject

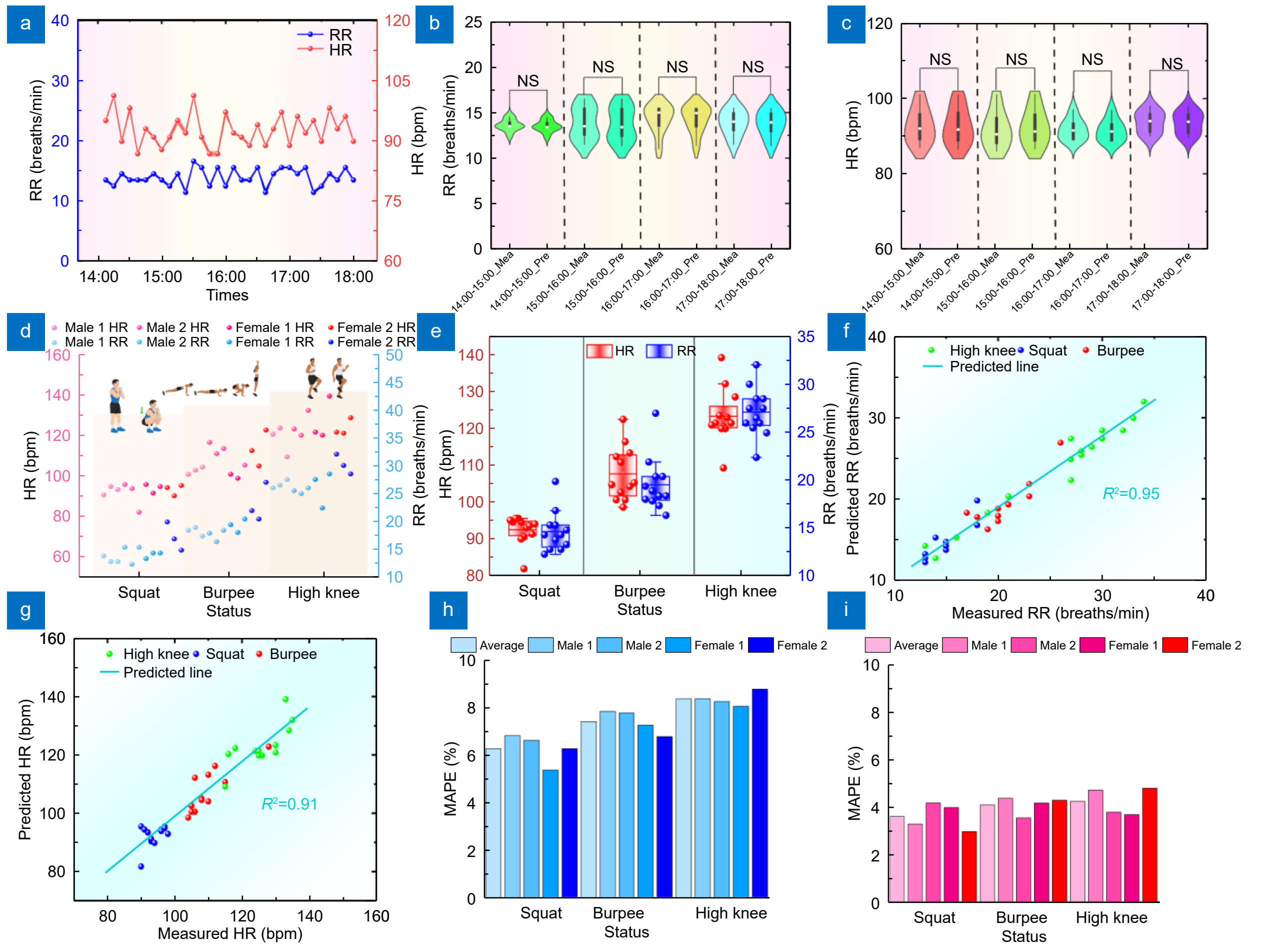

Fig. 7 | (**a**) RR and HR monitoring results at 14:00–18:00. (**b**) Violin plot comparing measured and reference RR results during 14:00–18:00, showing no significant difference and suggesting accurate continuous RR measurement. (**c**) Violin plot comparing measured and reference HR results during 14:00–18:00, showing no significant difference and suggesting accurate continuous HR measurement. (**d**) Scatter plot of RR and HR monitoring results of four subjects in squatting, burpee, and high knee. (**e**) Line box plot of RR and HR monitoring results of subjects in different statuses. (**f**) Correlation result plot between predicted and measured RR in different exercises. (**g**) Correlation result plots between the predicted and measured HR in different exercise states. (**h**) MAPE plot of RR predictions for subjects in different exercise states. (**i**) MAPE Plot of HR predictions of four subjects in different exercise states.

was selected for an in-depth longitudinal study. BP measurements were taken at three different times of the day-morning, afternoon, and evening-to observe the fluctuations in the subject's BP over the course of the day. In the final phase, where BP estimation is done under various conditions, the focus was on capturing the BP variations of the subjects during different physical states, including resting, squatting, and burpee. This phase aimed to assess the wristband's accuracy in detecting changes in BP under a range of physical conditions.

In these three phases, the seven distinct features extracted from the pulse wave signals, as described above, were utilized as the input to a GRU neural network. The objective of this neural network was to accurately estimate the subject's SBP and DBP. The smart wristband is equipped with a display screen to present the predicted BP values to the user. To confirm the accuracy of our measurements, SBP and DBP were also collected using a commercial sphygmomanometer (OMRON, T30J), which was worn on the radial artery as a reference standard. This measurement approach allowed us to validate the smart wristband's performance against a recognized medical device, ensuring the reliability of our findings. During the first experimental phase, a comprehensive dataset was collected, consisting of 300 sets of pulse wave signal features along with their corresponding SBP and DBP measurements. This dataset was obtained after the signal acquisition and preprocessing procedures described above. To visually represent the distribution of these BP, histograms were plotted for both SBP and

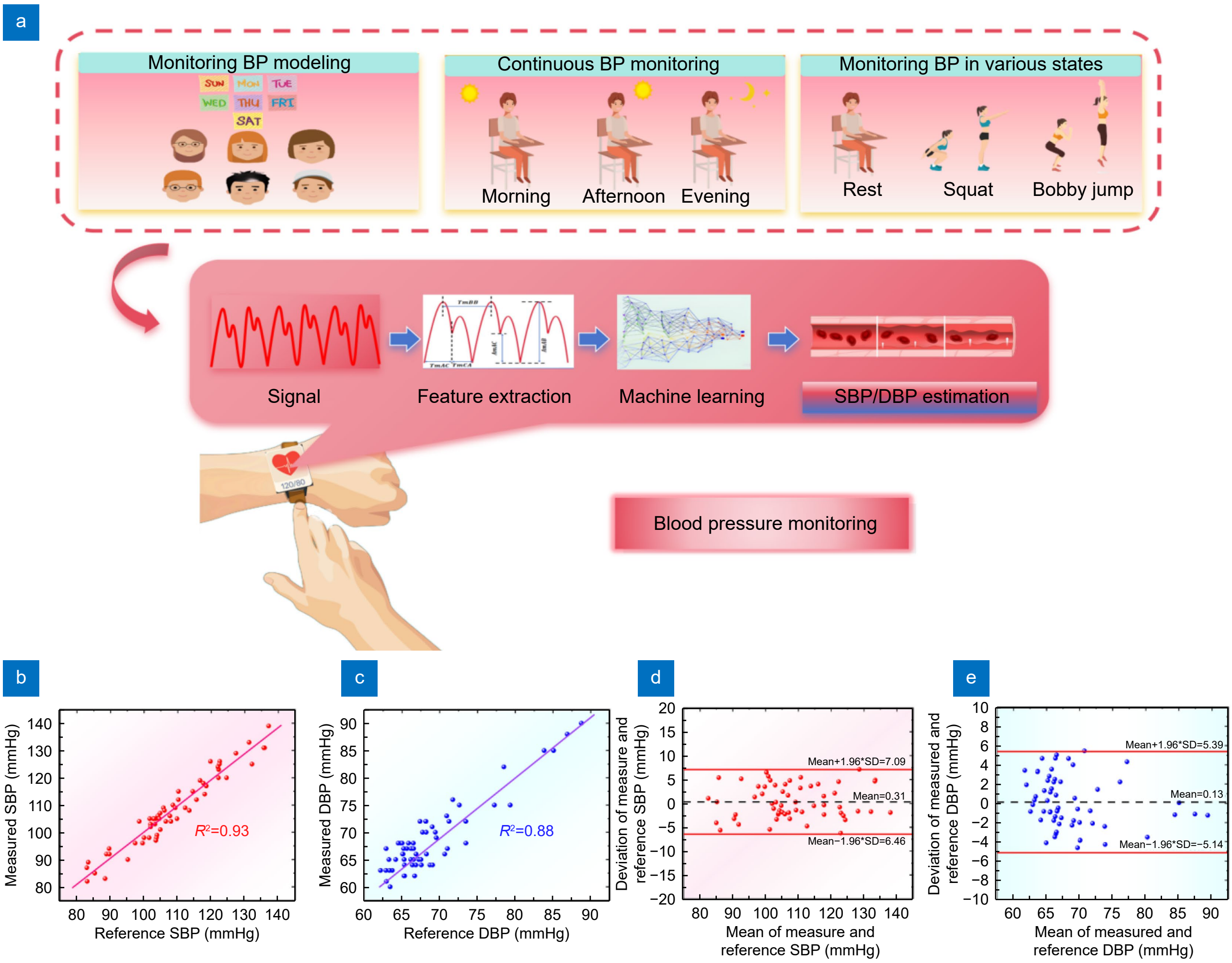

Fig. 8 | (**a**) Schematic diagram of three pivotal phases and BP estimation model processing the whole BP monitoring process is divided into six subjects to continuously monitor BP for one week to establish a model, another subject monitored BP changes in the morning, afternoon, and evening for one day, and another subject monitored BP fluctuations in different states (resting squat, burpee), the main model processing is divided into signal acquisition, feature extraction, and machine learning model estimation. (**b**) Correlation analysis graph between SBP measured results and reference results. (**c**) Correlation analysis plot of DBP measured results and reference results. (**d**) Bland-Altman plots of SBP, and (**e**) Bland-Altman plots of DBP.

DBP, as depicted in Fig. S4. We allocated 80% of the dataset as the training set to train the model, reserving the remaining 20% as the testing dataset to evaluate the model's performance. Figure 8(b) and 8(c) illustrate the correlation analysis between the measured and reference BP yielding R^2 of 0.93 for SBP and 0.88 for DBP, respectively. Additionally, Bland-Altman analysis (calculated by Eqs. (S4–S6)) is employed to assess the consistency between our wristband and the OMRON, T30J computing the deviation of measured and reference BP as mean ±1.96 standard deviations. The results of the error analysis are presented in Table S8. Specifically, the mean error for SBP was recorded at 0.31 mmHg, with a standard deviation of 3.45 mmHg, whereas the mean error for DBP was noted at 0.13 mmHg, with a standard deviation of 2.89 mmHg. According to the standards set by the Association for the Advancement of Medical Instrumentation (AAMI), which stipulate that the standard deviation must be less than 8 mmHg and the mean error must be less than 5 mmHg[67], the performance of our wristband device successfully meets these internationally recognized requirements. Furthermore, according to the criteria established by the British Hypertension Society, the error rates observed for our wristband device are comparable to those of Class A[68], thereby underscoring its full compliance with the relevant international standards.

As illustrated in Fig. 8(d) and 8(e), the Bland-Altman plots for both SBP and DBP reveal 95% confidence intervals of (−6.46 mmHg, 7.09 mmHg) for SBP and (−5.14 mmHg, 5.39 mmHg) for DBP. Crucially, all of the observed results fall within these respective 95% confidence intervals, thereby confirming that the blood pressure measurements obtained using our proposed wristband device are both accurate and consistent with those recorded by the OMRON T30J reference standard.

Subsequently, the BP of a subject (Gender: male; Height: 180 cm; Weight: 75 kg; BMI: 23.1) was continuously monitored over the course of the day, with measurements taken during morning, afternoon, and evening sessions, each lasting two hours. This comprehensive diurnal monitoring approach further validated the feasibility of our proposed wristband device to accurately track fluctuations in BP. For the purpose of reference, we compared the monitoring results obtained using our wristband against those recorded by the OMRON, T30J standard.

Figure 9(a) and 9(b) present the line graph and box chart of the BP measurement results, respectively. The line graph revealed that the participant's SBP was higher in the evening and lower in the morning, while the DBP was relatively lower in the evening. The box chart illustrated that the average SBP and DBP in the morning (9:00–11:00) were 98 mmHg and 67 mmHg, respectively. In the afternoon (15:00–17:00), the averages were 104 mmHg for SBP and 72 mmHg for DBP, In the evening (20:00–22:00), the averages were 106 mmHg for SBP and 69 mmHg for DBP, Fig. 9(c) and 9(d) displayed the correlation analysis between the measured and reference BP at different time points. The R^2 for the measured and reference SBP and DBP were 0.90 and 0.89, respectively. Furthermore, the Bland-Altman analysis, depicted in Fig. 9(e) and 9(f), evaluated the consistency of the measured BP. The mean error for SBP was 0.21 mmHg with a standard deviation of 3.52 mmHg and the 95% confidence intervals were (7.11 mmHg, −6.70 mmHg). For DBP, the mean error was 0.20 mmHg with a standard deviation of 2.22 mmHg, and the 95% confidence intervals were (4.63 mmHg, −4.22 mmHg). All test results essentially fell within the 95% confidence interval, indicating that our proposed wristband demonstrates excellent performance in continuously monitoring BP fluctuations. Moreover, the measurement results were consistent with the reference, showcasing the wristband's potential long-term, daily BP monitoring, offering a convenient solution for individuals seeking to maintain close observation of their BP. During the last experimental phase, an experiment was conducted with a subject to verify whether the proposed system could effectively monitor BP fluctuations under various conditions. The experiment involved monitoring the subject's BP in three distinct states: at rest, squats, and burpees. After the initial BP test of the subject in a relaxed state, he performed ten squats within a two-minute interval. After completing the squats, a 15-minute rest period was given to allow the subject's BP to return to its relaxed state. The final stage involved the subject performing ten burpees within two-minute intervals, in which BP measurements were taken. For reference, measured results from OMRON, T30J were used. This entire experimental procedure was repeated five times. The results are depicted in Fig. 9(g) and 8(h), which present the line graph and box plot of the experiment, respectively. Figure 9(g) illustrates that, compared to the resting state, BP gradually increased during the squatting exercise and also rose during the jumping exercise. Figure 9(h) shows that the average SBP and DBP at rest were 98 mmHg and 63 mmHg, respectively. During the squatting exercise, the averages increased to 109 mmHg for SBP and 71 mmHg for DBP, and during the jumping exercise, the averages further increased to 121 mmHg for SBP and 82 mmHg for DBP. These differences highlight the impact of varying exercise intensities on BP, with more strenuous activities leading to higher BP[69]. Additionally, Fig. 9(i) and 9(j) display the correlation coefficients for SBP and DBP, which were 0.91 and 0.93, respectively. The Bland-Altan analysis, illustrated in Fig. 8(k) and 8(l), evaluated the consistency of the measured BP, the mean error for SBP was −0.64 with a standard deviation of 2.54, and the 95% confidence intervals were (4.33, −5.62). For DBP, the mean error was −0.85 with a standard deviation of 2.49, and the 95% confidence intervals were (4.03, −5.74). The test results predominantly fell within the 95% confidence interval, indicating that the proposed wristband device is capable of accurately monitoring BP under different states. This demonstrates the wristband's effectiveness in capturing BP fluctuations, affirming its potential for monitoring BP under various conditions.

The three-phase experimental validation underscores several significant advantages of the smart wristband, including its high accuracy under varied conditions, capability for continuous monitoring of diurnal BP variations, and real-time monitoring functionality. The wristband's accuracy aligns with international standards, as previously detailed, and its user-friendly design is

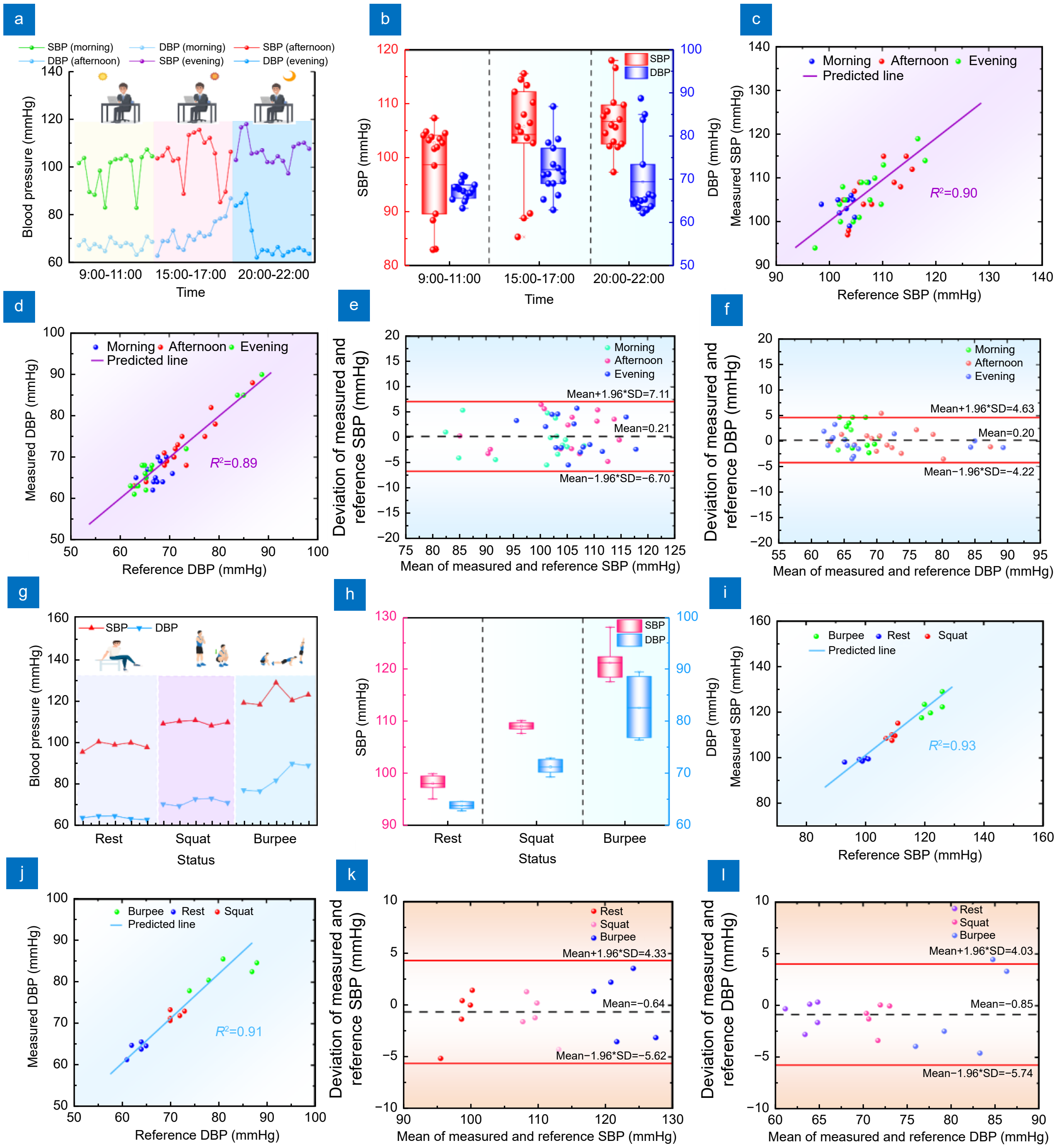

Fig. 9 | (**a**) Line graph of BP measurement results in the morning, afternoon, and evening. (**b**) Line box plots of BP measured results in the morning, afternoon, and evening. (**c**) Correlation analysis of SBP measured and reference results. (**d**) Correlation analysis of DBP measured and reference results. (**e**) Bland-Altman plot of SBP in the morning, afternoon, and evening. (**f**) Bland-Altman plot of DBP in the morning, afternoon, and evening. (**g**) Line graph of BP measurement results at rest, squat, and jump. (**h**) Line box plot of BP measurements at rest, squat, and burpee. (**i**) Correlation analysis of SBP measured and reference results under different exercise statuses. (**j**) Correlation analysis of DBP measured and reference results under different exercise states. (**k**) Bland-Altman plot of SBP at rest, squat, and burpee. (**l**) Bland-Altman plot of DBP at rest, squat, and burpee.

enhanced by the integrated display screen. These findings indicate that the smart wristband can play a crucial role in continuous cardiorespiratory function assessment and personalized healthcare services.

Biometric ID

Compared to current research that primarily focuses on a single aspect of cardiorespiratory function assessment, our smart wristband emphasizes functional diversity.

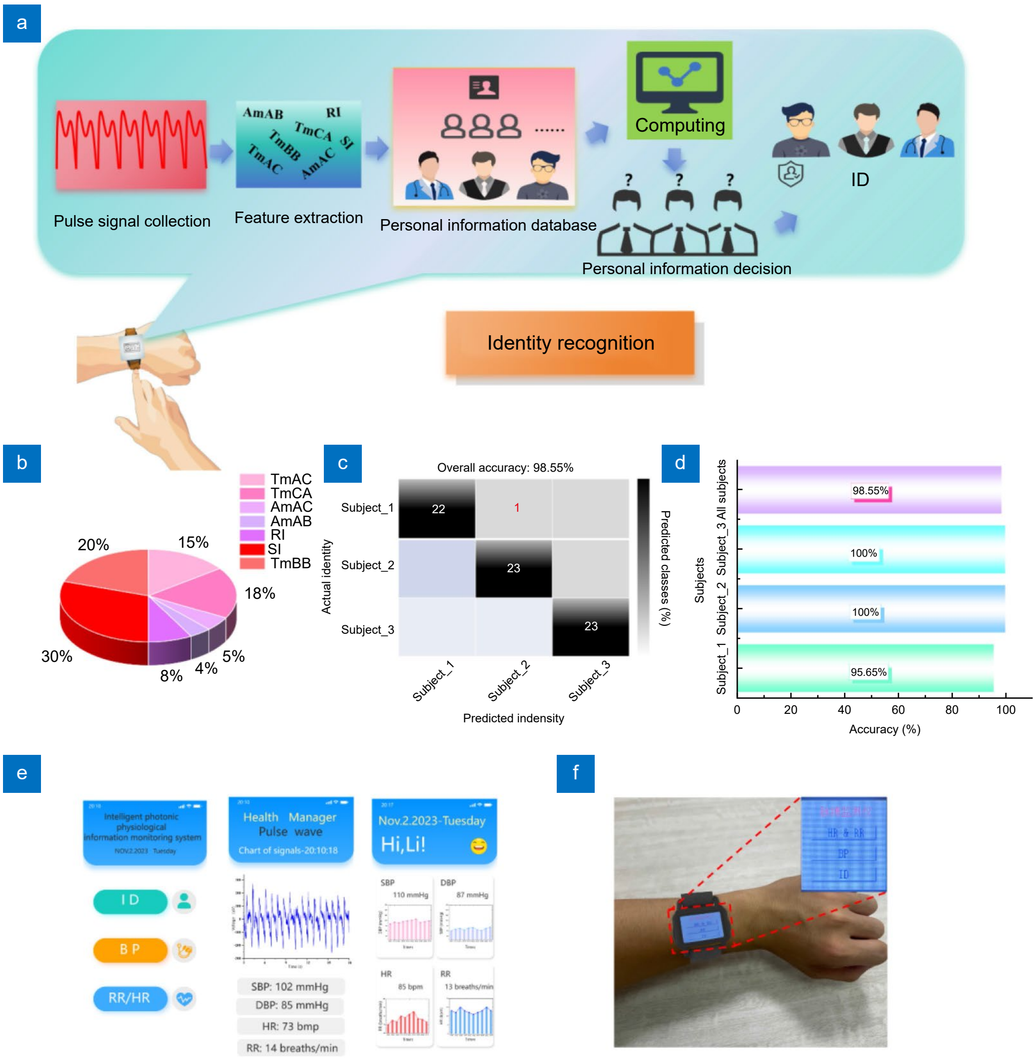

Fig. 10 | (**a**) Schematic diagram of the biometric identification process, which mainly includes pulse signal collection, pulse feature extraction, personal information database establishment, RF algorithm decision-making, and identification results. (**b**) The weighting pie chart of the seven features in the biometric identification process. (**c**) Confusion matrix for biometric identification results. (**d**) Biometric identification accuracy of different types of subjects and total prediction accuracy of three subjects. (**e**) The customized APP, a personal information interface, a week historical data interface, and a real-time measurement interface, and (**f**) The smartwatch worn by a 24-year-old male.

This work not only introduces a high-performance system for estimating RR, HR, and BP, but also incorporates biometric ID capabilities, which are essential for personalized healthcare services. As depicted in Fig. 10(a), the smart wristband worn on the left radial artery of the subjects, successively collects pulse wave signals. These high-precision and feature-rich pulse wave signals were processed through signal denoising and feature extraction techniques to obtain seven distinct pulse wave features. Subsequently, all the collected pulse wave features were compiled into a personal database. By integrating the personal information database with a well-trained classification RF model, the function of ID recognition was realized, with the result displayed on the screen, During the ID recognition process, the influence of external factors, such as body shape was considered. To acquire more representative pulse wave signals, three participants with different BMI values were selected for the experiments (see Supplementary Table S9) and the entire signal collection process was repeated over a total of three days. POLAR H10 was used as a reference device.

After completing the signal collection, preprocessing, and feature extraction procedures, a total of 345 feature data sets were obtained. Out of them, 80% were utilized for model training while the remaining 20% were reserved for model performance evaluation. As depicted in Supplementary Fig. S5, the loss of the RF model used for biometric ID rapidly converged after training with 300 decision trees. Figure 10(b) shows the feature weights of the seven pulse features during the RF model training process, with Stiffness Index (SI) accounting for 30% and time to Maximum Bubble Burst (TmBB) accounting for 20% of the total weight. Furthermore, two evaluation metrics were introduced to assess the test results: mean accuracy and recall, as defined in Eq. (S7–S8), respectively. The confusion matrix (Fig. 10(c)) and the accuracy bar chart (Fig. 10(d)) demonstrated that the ID model achieved an accuracy of 98.55% and a recall of 95.65%. These experimental results suggest that the proposed ID recognition method has the potential to prevent impersonation and effectively utilize intra-personal features for biometric identification. Notably, the ID recognition process was found to be unaffected by high BIM values, and the model recognition effects were excellent, laying a strong foundation for the development and of practical application of biometric technologies.

Concurrently, a customized mobile application (APP) program was developed to enhance user-friendliness, as shown in Fig. 10(e). This APP program features three key interfaces: a personal information interface, a weekly historical data interface, and a real-time measurement interface. These interfaces enable the real-time collection and analysis of health data, as well as biometric ID information. Furthermore, this APP holds significant potential in assisting individuals with cardiorespiratory diseases by providing a reference for monitoring their health conditions and evaluating the efficacy of their medication and treatment plans. As shown in Fig. 10(f), the smart wristband provides digital and personalized health monitoring information during the experiment.

Conclusion

In this work, we developed a photonic smart wristband based on the All-PSU hardware structure. Utilizing PSD analysis and machine learning techniques, precise cardiorespiratory function assessment and biometric identification have been achieved. The All-PSU hardware structure, characterized by its optical sensor and all-polymer design, exhibits high sensitivity and accuracy, ultrafast response and recovery times, remarkable long-term stability and durability effective waterproofing, and minimal positional drift. Through PSD analysis, the smart wristband achieved high accuracy in estimating RR and HR, with MAPE of 0.742% and 0.712% respectively. By employing machine learning methods, including GRU neural networks and RF algorithms, precise BP estimation and biometric ID have been achieved. The errors for SBP and DBP in daily conditions are 0.31±3.45 mmHg and 0.13±2.89 mmHg, respectively, while the biometric ID process achieved a correct rate of 98.55%. Beyond accuracy, the smart wristband demonstrated robustness across various application conditions and different BMI subjects, with continuous and real-time monitoring capabilities. Overall, in comparison to the existing work (presented in Table S10), the photonic smart wristband is a high-performance, functionally diverse wearable device, and we believe it can play a crucial role in personalized health services for the treatment and prevention of cardiorespiratory diseases in the future.

References

1. Timmis A, Vardas P, Townsend N et al. European society of cardiology: cardiovascular disease statistics 2021. *Eur Heart J* **43**, 716–799 (2022).
2. Pelliccia A, Sharma S, Gati S et al. 2020 ESC Guidelines on sports cardiology and exercise in patients with cardiovascular disease: the Task Force on sports cardiology and exercise in patients with cardiovascular disease of the European Society of Cardiology (ESC). *Eur Heart J* **42**, 17–96 (2021).
3. Lytras T, Mouratidou E, Andreopoulou A et al. Effect of early oseltamivir treatment on mortality in critically ill patients with different types of influenza: a multiseason cohort study. *Clin Infect Dis* **69**, 1896–1902 (2019).
4. Torres A, Cilloniz C, Niederman MS et al. Pneumonia. *Nat Rev Dis Primers* **7**, 25 (2021).
5. Lee JJ, Sundar KM. Evaluation and management of adults with obstructive sleep apnea syndrome. *Lung* **199**, 87–101 (2021).
6. Fuster V. High blood pressure guidelines: welcomed advice, but let's not lose the patient amid the numbers. *J Am Coll Cardiol* **71**, 800–801 (2018).
7. Zhang XK, Wang C, He DD et al. Identification of DNA methylation-regulated genes as potential biomarkers for coronary heart disease via machine learning in the Framingham Heart Study. *Clin Epigenetics* **14**, 122 (2022).
8. Couzin-Frankel J. Anti-inflammatory prevents heart attacks: by vindicating theory, antibody result points to new approaches to protecting the heart. *Science* **357**, 855 (2017).
9. Girard M, Deschamps J, Razzaq S et al. Emerging applications of extracardiac ultrasound in critically ill cardiac patients. *Can J Cardiol* **39**, 444–457 (2023).
10. Pujol-López M, San Antonio R, Mont L et al. Electrocardiographic optimization techniques in resynchronization therapy. *EP Eur* **21**, 1286–1296 (2019).
11. Zhang J, Fletcher JG, Harmsen WS et al. Analysis of heart rate and heart rate variation during cardiac CT examinations. *Acad Radiol* **15**, 40–48 (2008).
12. Meng KY, Xiao X, Wei WX et al. Wearable pressure sensors for pulse wave monitoring. *Adv Mater* **34**, 2109357 (2022).
13. Mohapatra D, Byun JE, Ansari MZ et al. Layer engineered MXene empowered wearable pressure sensors for non - invasive vital human–machine interfacing healthcare monitoring. *Adv Mater Technol* **8**, 2301175 (2023).

14. Meng KY, Xiao X, Liu ZX et al. Kirigami - inspired pressure sensors for wearable dynamic cardiovascular monitoring. *Adv Mater* **34**, 2202478 (2022).
15. Xiang ZH, Han MD, Zhang HX. Nanomaterials based flexible devices for monitoring and treatment of cardiovascular diseases (CVDs). *Nano Res* **16**, 3939–3955 (2023).
16. Han LY, Liang WJ, Xie QS et al. Health monitoring via heart, breath, and korotkoff sounds by wearable piezoelectret patches. *Adv Sci* **10**, 2301180 (2023).
17. Shi X, Zuo Y, Zhai P et al. Large-area display textiles integrated with functional systems. *Nature* **591**, 240–245 (2021).
18. Lee S, Franklin S, Hassani FA et al. Nanomesh pressure sensor for monitoring finger manipulation without sensory interference. *Science* **370**, 966–970 (2020).
19. Jiang YW, Zhang ZT, Wang YX et al. Topological supramolecular network enabled high-conductivity, stretchable organic bioelectronics. *Science* **375**, 1411–1417 (2022).
20. Wang DS, Li JP, Memik G. User identification based on finger-vein patterns for consumer electronics devices. *IEEE Trans Consum Electron* **56**, 799–804 (2010).
21. Xu W, Liu SD, Yang JY et al. Self-powered flexible handwriting input panel with 1D output enabled by convolutional neural network. *Nano Energy* **101**, 107557 (2022).
22. Maddirala G, Searle T, Wang X et al. Multifunctional skin-compliant wearable sensors for monitoring human condition applications. *Appl Mater Today* **26**, 101361 (2022).
23. Kireev D, Sel K, Ibrahim B et al. Continuous cuffless monitoring of arterial blood pressure via graphene bioimpedance tattoos. *Nat Nanotechnol* **17**, 864–870 (2022).
24. Li Z, Chen JX, Li LZ et al. Exceptional-point-enhanced sensing in an all-fiber bending sensor. *Opto-Electron Adv* **6**, 230019 (2023).
25. Feng HG, Chen X, Zhu RZ et al. Seeing at a distance with multicore fibers. *Opto-Electron Adv* **7**, 230202 (2024).
26. Liu HH, Hu DJJ, Sun QZ et al. Specialty optical fibers for advanced sensing applications. *Opto-Electron Sci* **2**, 220025 (2023).
27. Cai ZH, Li BZ, Bai ZY et al. Encrypted optical fiber tag based on encoded fiber Bragg grating array. *Int J Extreme Manuf* **5**, 035502 (2023).
28. Zhang L, Zhen YQ, Tong LM. Optical micro/nanofiber enabled tactile sensors and soft actuators: a review. *Opto-Electron Sci* **3**, 240005 (2024).
29. Pan J, Wang Q, Gao SK et al. Knot-inspired optical sensors for slip detection and friction measurement in dexterous robotic manipulation. *Opto-Electron Adv* **6**, 230076 (2023).
30. Jha R, Mishra P, Kumar S. Advancements in optical fiber-based wearable sensors for smart health monitoring. *Biosens Bioelectron* **254**, 116232 (2024).
31. Min R, Hu XH, Pereira L et al. Polymer optical fiber for monitoring human physiological and body function: a comprehensive review on mechanisms, materials, and applications. *Opt Laser Technol* **147**, 107626 (2022).
32. Guo JJ, Zhou BQ, Zong R et al. Stretchable and highly sensitive optical strain sensors for human-activity monitoring and healthcare. *ACS Appl Mater Interfaces* **11**, 33589–33598 (2019).
33. Zhu HT, Luo JX, Dai Q et al. Spatiotemporal hemodynamic monitoring via configurable skin-like microfiber Bragg grating group. *Opto-Electron Adv* **6**, 230018 (2023).
34. Chen MH, He YC, Liang HH et al. Stretchable and strain-decoupled fluorescent optical fiber sensor for body temperature and movement monitoring. *ACS Photonics* **9**, 1415–1424 (2022).
35. Tan FZ, Lyu WM, Chen SY et al. Contactless vital signs monitoring based on few-mode and multi-core fibers. *Opto-Electron Adv* **3**, 190034 (2020).
36. Guo JJ, Niu MX, Yang CX. Highly flexible and stretchable optical strain sensing for human motion detection. *Optica* **4**, 1285–1288 (2017).
37. Li LY, Liu YF, Song CY et al. Wearable alignment-free microfiber-based sensor chip for precise vital signs monitoring and cardiovascular assessment. *Adv Fiber Mater* **4**, 475–486 (2022).
38. Zhu HT, Zhan LW, Dai Q et al. Self - assembled wavy optical microfiber for stretchable wearable sensor. *Adv Opt Mater* **9**, 2002206 (2021).
39. Pang YN, Liu B, Liu J et al. Singlemode-multimode-singlemode optical fiber sensor for accurate blood pressure monitoring. *J Light Technol* **40**, 4443–4450 (2022).
40. Li LY, Sheng SF, Liu YF et al. Automatic and continuous blood pressure monitoring via an optical-fiber-sensor-assisted smartwatch. *PhotoniX* **4**, 21 (2023).
41. Wang YK, Yu XL, Jiang CL et al. Micro-nano fiber flexible multimodal sensors for fingerprint recognition. *IEEE Sens J* **24**, 4504–4509 (2024).
42. Li JH, Chen L, Yan XP et al. Super-stretchable polymer optical fibers for robot finger posture and pressure recognition. *J Light Technol* (2024), doi: 10.1109/JLT.2024.3519531.
43. Wang Z, Chen ZY, Ma L et al. Optical microfiber intelligent sensor: wearable cardiorespiratory and behavior monitoring with a flexible wave-shaped polymer optical microfiber. *ACS Appl Mater Interfaces* **16**, 8333–8345 (2024).
44. Kuang RF, Wang Z, Ma L et al. Smart photonic wristband for pulse wave monitoring. *Opto-Electron Sci* **3**, 240009 (2024).
45. Leal-Junior A, Avellar L, Biazi V et al. Multifunctional flexible optical waveguide sensor: on the bioinspiration for ultrasensitive sensors development. *Opto-Electron Adv* **5**, 210098 (2022).
46. Wang LL, Zhong C, Ke DN et al. Ultrasoft and highly stretchable hydrogel optical fibers for in vivo optogenetic modulations. *Adv Opt Mater* **6**, 1800427 (2018).
47. Zha BJ, Wang Z, Ma L et al. Intelligent wearable photonic sensing system for remote healthcare monitoring using stretchable elastomer optical fiber. *IEEE Internet Things J* **11**, 17317–17329 (2024).
48. Rendeiro R, Jargus J, Nedoma J et al. The possibilities of using a mixture of PDMS and phosphor in a wide range of industry applications. *Opto-Electron Adv* **7**, 240133 (2024).
49. Jakubowski K, Huang CS, Boesel LF et al. Recent advances in photoluminescent polymer optical fibers. *Curr Opin Solid State Mater Sci* **25**, 100912 (2021).
50. Li TL, Wang QA, Su YF et al. AI-assisted disease monitoring using stretchable polymer-based sensors. *ACS Appl Mater Interfaces* **15**, 30924–30934 (2023).
51. Fan XY, Huang Y, Ding XR et al. Alignment - free liquid - capsule pressure sensor for cardiovascular monitoring. *Adv Funct Mater* **28**, 1805045 (2018).
52. Fu Y, Zhao S, Wang LQ et al. A wearable sensor using structured silver - particle reinforced PDMS for radial arterial pulse wave monitoring. *Adv Healthc Mater* **8**, 1900633 (2019).
53. Song ZQ, Li WY, Bao Y et al. Bioinspired microstructured pressure sensor based on a janus graphene film for monitoring vital

signs and cardiovascular assessment. *Adv Electron Mater* **4**, 1800252 (2018).

54. Li YJ, Wang ZL, Zhang L et al. Characters available in photoplethysmogram for blood pressure estimation: beyond the pulse transit time. *Australas Phys Eng Sci Med* **37**, 367–376 (2014).
55. Ding M, Zhou H, Xie H et al. A gated recurrent unit neural networks based wind speed error correction model for short-term wind power forecasting. *Neurocomputing* **365**, 54–61 (2019).
56. Wang YS, Xia ST, Tang QT et al. Novel consistent random forest framework: Bernoulli random forests. *IEEE Trans Neural Netw Learn Syst* **29**, 3510–3523 (2018).
57. Liu YC, Li HY, Liang XP et al. Speech recognition using intelligent piezoresistive sensor based on polystyrene sphere microstructures. *Adv Intell Syst* **5**, 2200427 (2023).
58. Yu ZC, Xu JH, Gong HX et al. Bioinspired self-powered piezoresistive sensors for simultaneous monitoring of human health and outdoor UV light intensity. *ACS Appl Mater Interfaces* **14**, 5101–5111 (2022).
59. Mizuno R, Fujimoto S, Nakano H et al. Atrial conduction abnormalities in patients with systemic progressive sclerosis. *Eur Heart J* **18**, 1995–2001 (1997).
60. Mejía-Mejía E, May JM, Elgendi M et al. Differential effects of the blood pressure state on pulse rate variability and heart rate variability in critically ill patients. *Npj Digit Med* **4**, 82 (2021).
61. Favilla R, Zuccalà VC, Coppini G. Heart rate and heart rate variability from single-channel video and ICA integration of multiple signals. *IEEE J Biomed Health Inform* **23**, 2398–2408 (2019).
62. Peetermans M, Guler I, Meersseman P et al. Impact of BMI on outcomes in respiratory ECMO: an ELSO registry study. *Intensive Care Med* **49**, 37–49 (2023).
63. Boehmer J, Mark G, Wen GZ et al. Impact of body mass index on device measured diagnostic sensor measurements in ambulatory heart failure patients. *J Card Fail* **24**, S128–S129 (2018).
64. Guo X, Wang Y, Zhou NW et al. Optimal weighted two-sample *t*-test with partially paired data in a unified framework. *J Appl Stat* **48**, 961–976 (2021).
65. Dominelli PB, Archiza B, Ramsook AH et al. Effects of respiratory muscle work on respiratory and locomotor blood flow during exercise. *Exp Physiol* **102**, 1535–1547 (2017).
66. Chan PY, Ryan NP, Chen D et al. Novel wearable and contactless heart rate, respiratory rate, and oxygen saturation monitoring devices: a systematic review and meta‐analysis. *Anaesthesia* **77**, 1268–1280 (2022).
67. Luo H, Yang DY, Barszczyk A et al. Smartphone-based blood pressure measurement using transdermal optical imaging technology. *Circ Cardiovasc Imaging* **12**, e008857 (2019).
68. Hermányi Z, Pokoly B, Visolyi G et al. Evaluation of meditech ABPM-06 ambulatory blood pressure measuring device, according to the European Society of Hypertension, the British Hypertension Society and the International Organization for Standardization protocol. *Blood Press Monit* **24**, 208–211 (2019).
69. Debray A, Ravanelli N, Chenette-Stewart O et al. Effect of exercise training on blood pressure in healthy postmenopausal females: a systematic review with meta-analysis. *Med Sci Sports Exerc* **55**, 1317–1325 (2023).

Acknowledgements

This research funded by the National Key R&D Program of China(2022YFE0140400); the National Natural Science Foundation of China(62405027, 62111530238, 62003046); Supporting project of major scientific research projects of Beijing Normal University at Zhuhai (ZHPT2023007); The work of R.Min was supported by the Tang Scholar of Beijing Normal University.The research was co-funded by the financial support of the European Union under the REFRESH – Research Excellence For REgion Sustainability and High-tech Industries project number CZ.10.03.01/00/22003/0000048 via the Operational Programme Just Transition. This work was developed within the scope of the projects CICECO-Aveiro Institute of Materials, UIDB/50011/2020 (DOI 10.54499/UIDB/50011/2020), UIDP/50011/2020 (DOI 10.54499/UIDP/50011/2020) & LA/P/0006/2020 (DOI 10.54499/LA/P/0006/2020) financed by national funds through the FCT/MCTES (PIDDAC).

Author contributions

W. L.,C. M., and R. M. conceived the project idea and designed the experiments.W. L., Y. L., Y. Y., and Z. W. carried out the experiments and collected the data. W. L., and K. X. contributed to sensor fabrication and cardiorespiratory monitoring experiment. Z. W., Y. L., D. Z., and X. L. contributed to behaviour monitoring experiment. W. L., R. M., S. K., B. O. and C. M. analysed all the data and cowrote the paper. All authors discussed the results and commented on the manuscript.

Competing interests

The authors declare no competing financial interests.

Supplementary information

Supplementary information for this paper is available at
https://doi.org/10.29026/oea.2025.240254

Scan for Article PDF